The 8th European Congress on Computational Methods in Applied Sciences and Engineering
ECCOMAS Congress 2022
5-–9 June 2022, Oslo, Norway

KRUEGER HIGH-LIFT SYSTEM DESIGN OPTIMIZATION

Emiliano Iuliano[1], Domenico Quagliarella[2] and Jochen Wild[3]

[1] Italian Centre for Aerospace Research (CIRA)
Via Maiorise, Capua, Italy
currently at Lilium eAircraft GmbH
Claude-Dornier Str. 1, Geb. 335, 82234 Wessling, Germany
e-mail: emiliano.iuliano@lilium.com

[2] Italian Centre for Aerospace Research (CIRA)
Via Maiorise, Capua, Italy
email: d.quagliarella@cira.it

[3] German Aerospace Center (DLR)
Inst. of Aerodynamics and Flow Technology
Braunschweig, Germany
email: jochen.wild@dlr.de

Key words: High-lift aerodynamics, High-lift system design, Design optimization

Abstract. This work describes the cooperative/competitive design process that led to the definition of the Krueger flap to be used in the numerical and experimental tests of the European project UHURA. The project requirements are particularly challenging because it is necessary to develop a device with good aerodynamic high-lift characteristics, but it is necessary to consider many constraints of structural and kinematic nature. Indeed, the kinematics for its deployment is quite complex and imposes hard constraints on the Krueger shape, and the structural characteristics must allow it to withstand considerable structural stresses in the deployment phase which is studied in the wind tunnel.

1 INTRODUCTION

Within the EU UHURA project [1], the need emerged to design a folding bull nose Krueger device as the target configuration for studying unsteady aerodynamic effects during deployment and retraction of such a system. Consequently, the design objective of generating as much as possible lift force was subject to the heavy and demanding constraint of being adequately integrated into existing wind tunnel models. Hence, the design specifications require a high-performance Krueger device that doesn't exhibit artificial flow effects besides offering high-performance. This constraint is more important than getting the ultimate performance in terms of maximum lift. As a starting point, the design experience obtained in previous projects, DeSiReH [2] and AFLoNext [3], has been used to generate an initial Krueger shape. Hence, the characteristic design parameters of the Krueger device obtained in DeSiReH have been mapped to the DLR-F15-LLE geometry [4]. The design of the Krueger flap has been obtained by a cooperative concurrent engineering approach between two UHURA partners, namely CIRA

and DLR, in an iterative process. In a first loop, independent optimizations were performed based on the partner's best practice methods. Afterwards, the designs were merged by selecting beneficial aspects of both optimization results. Finally, the design was adapted to respect refined kinematics constraints. The synthesized design achieves all requirements from kinematics and achieves a high level of maximum lift coefficient. For the final design, aerodynamic forces have been derived for the Krueger panel and the bull-nose to support kinematics sizing.

2 KRUGER DEVICE SHAPE OPTIMIZATION

The design of the Krueger flap has been obtained by a cooperative concurrent engineering approach with two UHURA partners, CIRA and DLR, involved. Based on a common design case definition and requirements, in an iterative process a common design has been created. In a first loop independent optimizations were performed based on partner's best practice methods. Afterwards the designs were merged by selecting beneficial aspects of both optimization results. Finally the design was adapted to respect refined constraints, especially from kinematics feasibility requirements.

2.1 Initial krueger device shape

Thi initial Krueger flap design, reported in Figure 1 is derived from the AFLoNext design parameters mapped on DLR-F15-LLE airfoil. Initial side constraints taken from the AFLoNext project were the front spar clearance and the shielding requirement against 7° impact at 6° angle of attack.

Figure 1: initial Krueger flap design.

The design variables from AFLoNext result in a Krueger flap with a deflection angle close to the upper limit of $\delta_K = 150°$. The swallow setting originates from a relatively thin leading edge and the strong shielding requirement. The initial Krueger flap shape has been provided via Coordination Memorandum UH-11-CM03-DLR [4].

2.2 Design case definition

The design case specification was made to explore the broadest possible design space. Hence, the degrees of freedom for the design of the Krueger flap incorporate all shape variables for the bull nose and the inner panel shape. The Krueger flap is selected as a folding bull nose device as this incorporated a higher degree of freedom for the Krueger leading edge shape and avoids the necessity of additional devices to seal the Krueger cavity in retracted position.

2.2.1 Design targets and requirements

The target of the design is to obtain a reasonable Krueger flap shape that incorporates a highly loaded Krueger flap for high maximum lift coefficient based on a feasible gooseneck kinematics. The Krueger angle should not be too shallow in order to prevent premature separation on the upper side of the Krueger. As the Krueger flap is intended for a laminar wing airfoil, the Krueger position must achieve a position that prevents insect contamination during take-off and landing. The initial Krueger shielding was first taken from the AFLoNext project to prevent an impact of an insect with 7° relative to the surface tangent at an angle of attack of 7°. Figure 2 depicts the geometric interpretation of this design target.

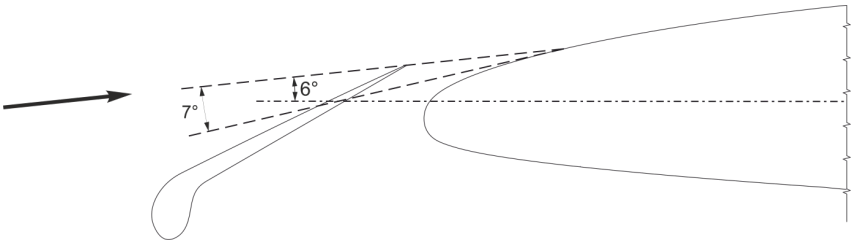

Figure 2: geometric representation of the insect shielding requirement.

2.2.2 Design constraints

The size of the Krueger flap is limited by a request on a front spar clearance of 0.5%c. Additionally due to the type of kinematics, there is an implicit fixation of the panel trailing edge resulting from the designated setting in deflection position and the hinge line position. The hinge line is hereby restricted to be not closer than 0.556%c to the upper shell shape to allow for bearings to mount the kinematics. Figure 3 shows the relations of these limitations.

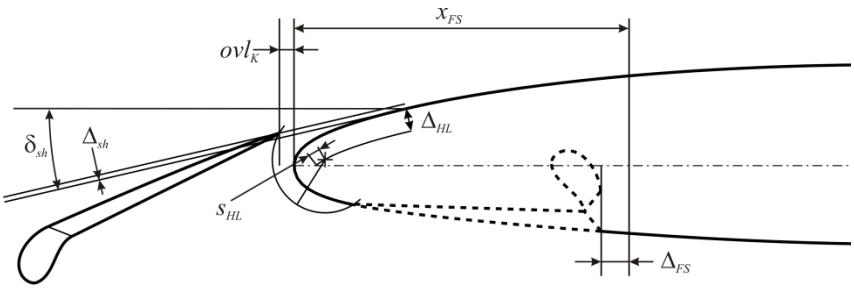

Figure 3: limitation of Krueger panel size implicitly from kinematics type and target setting.

For the bull nose shape, a side constraint is given on the size of the cavity. In order to maintain structural integrity, the cavity needed to store the Krueger shall not extend 40% of the local airfoil thickness at any position.

2.3 DLR design

DLR used its validated numerical optimization environment CHAeOPS in conjunction with the RANS CFD solver FLOWer [5]. Computational multi-block structured grids are generated by a parametric procedure that achieves self-similar mesh qualities throughout the design space. The mesh consists of 10 blocks with a total of 151,162 grid points. The mesh resolution is adopted for viscous flows to achieve a non-dimensional wall distance of the first cell in the field in the order of $y^+ = 1 \div 2$.

The flow solver FLOWer is a standard finite volume method to solve the Reynolds-averaged Navier-Stokes (RANS) equations. It applies a 2^{nd} order central flux discretization with artificial dissipation. Steady state solutions are obtained by an explicit 5-stage Runge-Kutta time stepping scheme accelerated by implicit residual smoothing, local time stepping and a 3-level multigrid. For turbulent viscous flow the closure of the RANS equations is obtained by application of the one-equation Spalart-Almaras turbulence model modified by Edwards and Chandra. The turbulence equation is solved by a fully implicit scheme. In order to speed-up the optimization, the RANS calculations during the optimization have been computed on a coarser mesh obtained as the 2^{nd} multigrid level.

The computational grid is a multi-block grid consisting of 10 structured blocks. The mesh consists of about 150,000 grid points. The boundary layer is resolved by boundary conforming meshes with a high density normal to the wall with at least 32 layers to resolve the boundary layer. The first wall spacing is adopted to the designated Reynolds number to achieve a non-dimensional wall distance of $y^+ = 1 \div 5$. The farfield boundary is located at 10 airfoil chord lengths as the solver features a farfield vorticity correction based on the circulation produced by the airfoil.

Figure 4 depicts the geometric relation of the design parameters used in the optimization process. Together with the parameters for the hinge line coordinate and the front spar clearance shown in Figure 3, 12 parameters in total are used to fully describe the geometry. As stated above, the length of the Krueger panel and the deflection angle are no direct parameters but result from the feasibility constraints of the kinematics and the designated trailing edge location in deflected position. For the panel the free shape parameter is the thickness at the junction to the bull nose. The bull nose shape is defined by four parameters defining the size and the position of the extrema in local coordinates. The extrema are GC1-continuously connected by cubic splines to the Krueger panel shape.

The optimization has been aimed at two objectives relating to first order aircraft performance indicators in high-lift flight condition. The first objective has been to minimize the stall speed V_S by maximizing the maximum section lift coefficient $c_{L,\max}$.

$$f_1 = -c_{L,\max} \ @ \ M_\infty = 0.19 \tag{1}$$

The second objective has been a performance increase to maximize the climb speed inidicated by the climb ratio based on section data

$$f_2 = \frac{c_D^2}{c_L^3} \ @ \ M_\infty = 0.2337 \ (\hat{=}1.23 \times V_S) \tag{2}$$

The optimization method applied was a mono-objective simplex method with subspace division. The single objective has been constructed by an addition of both objectives with weights

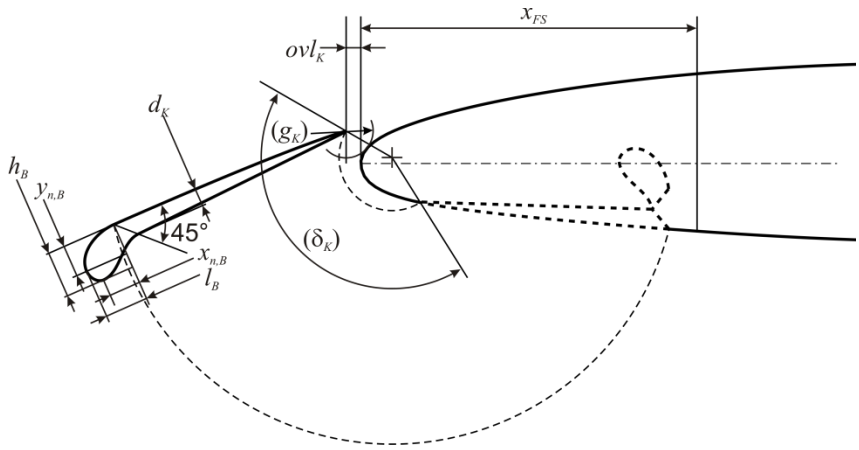

Figure 4: Geometric parameterization of the Krueger flap applied in the DLR design optimization

attempting an approximately equal influence. A first optimization was run starting with the baseline configuration and a global objective of

$$F_{\text{obj}} = f_1 + 1000 \cdot f_2 \tag{3}$$

The maximum lift iterations were started at an angle of attack of 15.5°. After 160 RANS evaluations it turned out that in the optimized configurations the maximum lift was not properly detected due to a too high starting angle of attack. The starting angle of attack was reduced to 11°. Additionally, due to the improvements obtained that far, the objective function was misbalanced to favour maximum lift only as the high drag values of the initial configuration resulting from flow separations disappeared. Therefore the global objective has been refined to

$$F_{\text{obj}} = f_1 + 10000 \cdot f_2 \tag{4}$$

The final optimization then needed 6 optimization cycles performing 330 RANS evaluations of different configurations at a wall time of 444 hours on a single workstation. Table 1 lists the changes in the objective functions. Figure 5 depicts the changes in the geometry. It is seen that the optimized Krueger is much more steeply deflected. Additionally, the bull nose significantly increased in size and exhibited a smooth curvature. The Krueger panel length is approximately similar, which is better observed when inspecting the resulting cavity in the wing.

For analysis of performance and loads, the full polar curve has been simulated on the fine grid. Figure 6 shows a comparison of the lift coefficient versus the angle of attack of the initial and the optimized configuration. Due to the swallow Krueger deflection of the initial configuration, the lift curve exhibits an early separation due to flow separation over the Krueger flap, which is successfully prevented with the optimized design parameters. The optimized configuration exhibits a maximum section lift coefficient of $c_{L,\max} = 4.527$ at an angle of attack of $\alpha = 26°$. In the linear range, there is only a slight drop in lift coefficient compared to the initial configuration. Such high performance is promising as it is very similar to those of a classical slat device, especially with regard to the swallow trailing edge flap deflection.

ID airfoil	Spalart-Allmaras		
	F_{obj}[1]	f_1	f_2
Baseline	-0.0572	-2.7331	2.6759×10^{-5}
intermediate-optimum	-2.2568	-3.4162	1.1594×10^{-5}
final-optimum	-3.4851	-4.3271	0.8420×10^{-5}

[1] In the table, the values of the global objective are based on the final weighting.

Table 1: Summary of DLR optimization results.

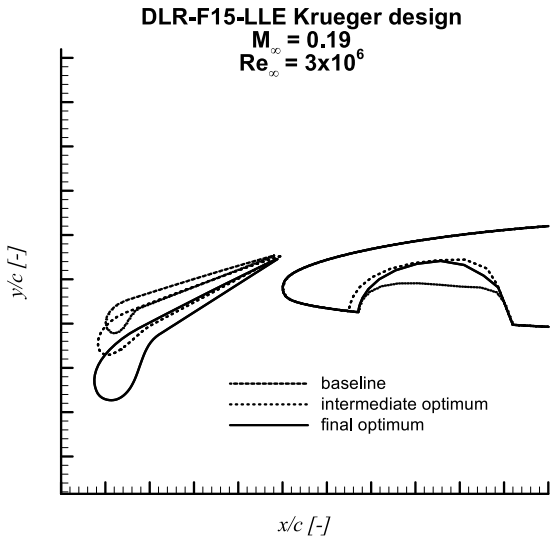

Figure 5: Comparison of the shapes of the Krueger flap for the initial, an intermediate and the finally optimized configuration of the DLR design optimization

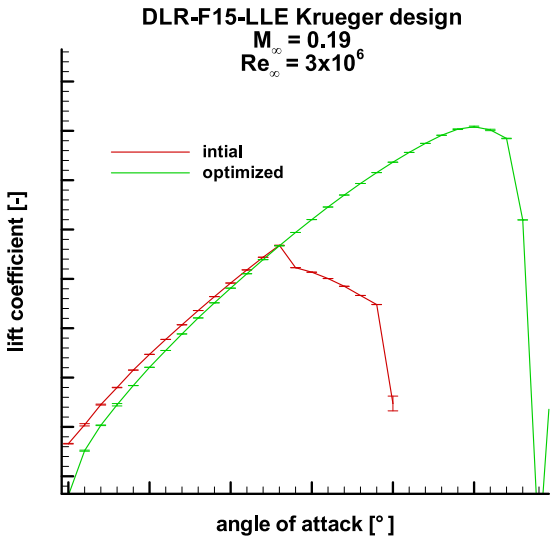

Figure 6: Comparison of lift coefficient versus angle of attack for the initial and optimized configuration of the DLR design optimization

2.4 CIRA design

CIRA was in charge of defining the shape of the Krueger element side by side with DLR. As the focus was on designing the Krueger shape compatibly with stowing and kinematic constraints, a dedicated CAD-free geometric parameterization was implemented to allow for feasible panel length and deployment handling. Then, a numerical optimization task was performed to improve the high-lift performance of the baseline shape. In the following sections, details are provided about both activities.

2.4.1 Geometry parameterization and constraints handling

The shape of the Krueger element was strongly constrained as defined in 2.2.2 to meet kinematics and deployment considerations. Consequently, CIRA geometry parameterization has been tailored to this specific problem at hand. With reference to Figure 7, Figure 8 and

Figure 10, a parametric CAD-free procedure has been setup consisting of the following steps:

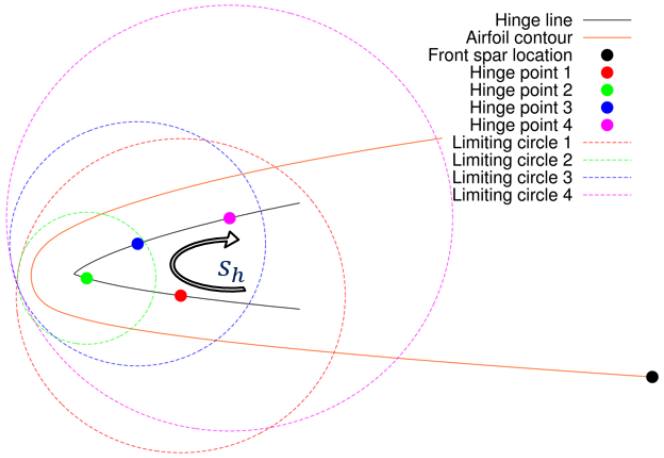

Figure 7: Offset hinge line, hinge point locations and corresponding limiting circles

Hinge point stay-in line and location — the constrained hinge line is parameterized as a curve, and the hinge point location is taken as the corresponding curvilinear abscissa (s_h, ranging from 0 to 1, where 0 and 1 identify the lower and upper limit, respectively, and 0.5 identifies the cuspid at leading edge, see Figure 7);

Krueger panel forward limit — in order to avoid the clash of the Krueger trailing edge with the pointy wing leading edge during the deployment, a limiting circle is drawn, representing the trajectory of the Krueger element trailing edge during the deployment phase. The circle is centered in the hinge point and tangent to the leading edge. The radius is increased of an additional $0.005\%c$ in order to assure a minimal clearance during the deployment. Figure 7 shows various choices for hinge point and corresponding limiting circles;

Krueger panel definition — the Krueger outer panel (in retracted position) is automatically defined by the parameter s_h. Indeed, the panel aft limit is represented by the front spar position, the forward limit by the intersection of the limiting circle with the airfoil contour;

Baseline shape in retracted position - the (reference) bullnose shape is attached to the Krueger panel in retracted position and the Kruger inner panel is defined as a line segment connecting the bullnose to the trailing edge (see Figure 8);

Bullnose shape modification — the bullnose shape is locally modified as $y_m(x) = y_b(x) + \sum_{i=1}^{4} w_i f_i(x)$, where $y_m(x)$ is the modified shape, $y_b(x)$ is the baseline reference shape, w_i are the shape control parameters and $f_i(x)$ are sinusoidal Hicks-Henne bump functions: $f_1(x) = 0.1\sin^3\left(\pi x^{0.431}\right)$, $f_2(x) = 0.1\sin^3\left(\pi x^{0.757}\right)$, $f_3(x) = 0.1\sin^3\left(\pi x^{1.357}\right)$, $f_4(x) = 0.1\sin^3\left(\pi x^{3.106}\right)$. Figure 9 shows an example of the geometry modifications introduced by applying the bump functions one by one. The range of variation of the weights are chosen in such a way as to keep the bullnose height within the limit imposed by the stowage space in retracted position (around 40 % of the main airfoil thickness). As it will be detailed in the following sections, this aspect represents an important trade-off between the achievable aerodynamic performance and the allocation of the Krueger device.

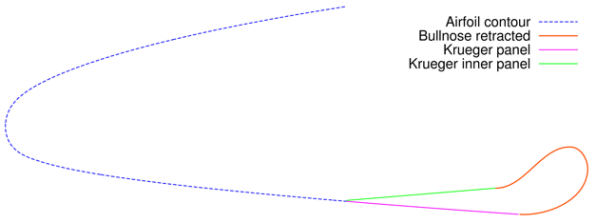

Figure 8: Definition of the Krueger geometry in retracted position. The outer panel (purple line) is defined according to the kinematic constraints, the reference bullnose shape (red line) is connected to it and the inner panel is defined as a line segment (green line).

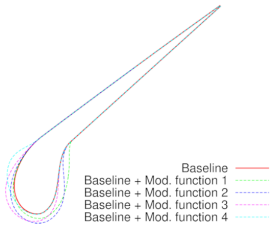

Figure 9: Reference bullnose shape modified by selected Hicks-Henne functions.

Modified shape in deflected position — the entire Krueger shape, modified as aforementioned, is then rotated about the hinge point by an angle δ which varies according to the hinge point location so as to satisfy the shielding requirement. With reference to Figure 10, δ is the angle identified by the intersections of the limiting circle with the lower airfoil contour (Krueger panel trailing edge) and the shielding line (purple line) respectively. By construction, there exists a range of values of s_h which do not allow to satisfy the shielding constraint (no intersection between the limiting circle and the shielding line) or to reach it with a feasible rotation ($\delta < 150°$). The allowed range is found to be $s_h \in [0.55, 1.0]$, i.e. the hinge point should stay on the upper branch of the hinge line and far enough from the leading edge cuspid. This consideration is directly exploited to set the range of variation of the hinge point in the optimization loop.

The total number of design parameters is 5: the s_h parameter controls the panel length, the deflected Krueger setting and gap/overlap (in accordance with the shielding constraint), while the 4 parameters w_i controls the bullnose shape.

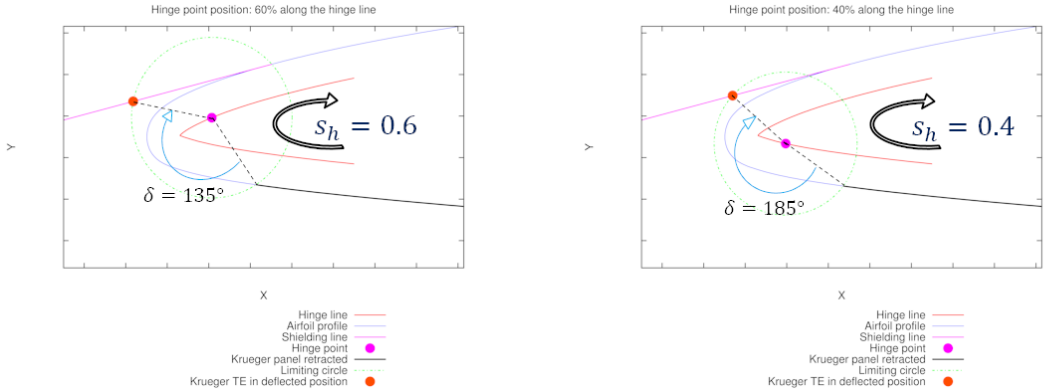

Figure 10: How the hinge point location and shielding angle constraints determine the Krueger trailing edge deflected position.

2.4.2 Shape optimization problem definition

The shape optimization problem is aimed at improving the performance of the three-element configuration in high-lift conditions at single design point $\left(M_\infty = 0.15, \Re_\infty = 7 \times 10^6\right)$. The reference length for airfoil coefficients calculation is based on the projected length onto the X-axis in deflected position ($= 1.37m$ for unit chord airfoil). Instead of considering only the maximum lift coefficient as objective, a quite different approach has been adopted to improve the aerodynamic performance along a selected branch of the lift curve. With reference to Figure 11, two "utopia" points (red lines) have been identified for lift and drag coefficients, namely $c_L^* = 3.2$ and $c_D^* = 0.0300$, as well as a window of observation for the angle of attack defined by $\alpha_l = 14°$ and $\alpha_u = 24°$ (lower and upper bounds, respectively). The objective function is evaluated as:

$$f_{\text{obj}} = \int_{\alpha_l}^{\alpha_u} \left[(c_L^* - c_L) + 10\,(c_D - c_D^*)\right] \mathrm{d}\alpha = \mu\,(\Omega_L) + 10\mu\,(\Omega_D) \tag{5}$$

where μ is the area of the green domains in Figure 11 and the weight 10 on the drag contribution has been set to give it the proper importance. In other words, such a choice of the objective function rewards both an increase in $c_{L,\max}$ and a better lift characteristic while approaching the stall condition. On the other hand, taking into account the drag performance allows penalizing the onset of separated regions. The angle of attack range $[\alpha_l, \alpha_u]$ has been discretized in steps of $\Delta\alpha = 2°$ in order to reduce the total number of CFD simulations and save computational time.

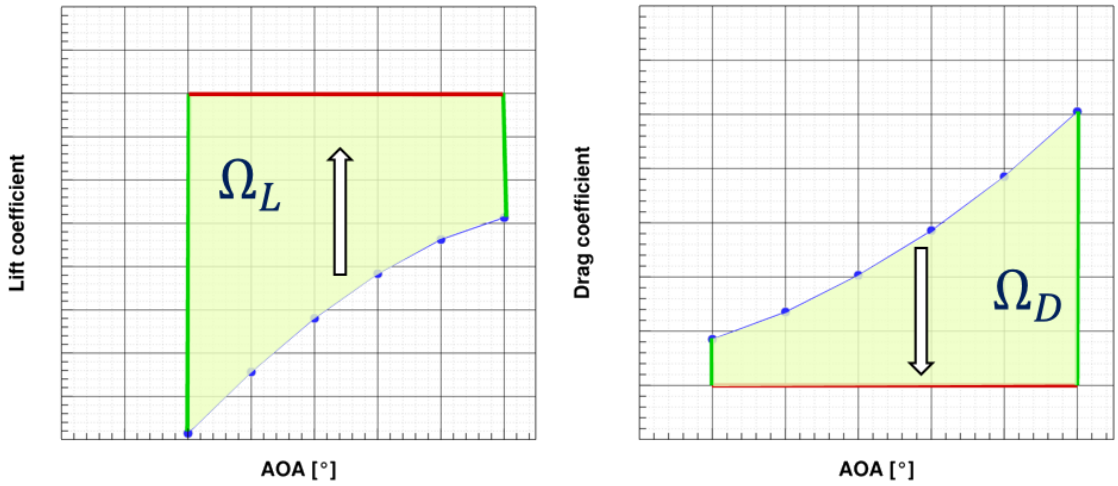

Figure 11: Measure of lift and drag curve domains for objective function computation.

2.4.3 Shape optimization process and results

An automatic meshing procedure has been prepared in order to obtain fixed-quality meshes around varying geometries. The procedure employs the GMSH open-source tool [6] to generate

mixed quad-tri meshes. The minimum triangle element size is 0.00075 (with respect to unit chord airfoil), while the farfield is a square box located at 40 airfoil chords from the main element leading edge and its element size is set to 6. A distance-based refinement is employed near the airfoil surface, enabling a smooth transition from near-wall to farfield elements. A boundary layer region (quad layers) is attached around the solid surfaces by specifying the approximate boundary layer height (estimated by means of Schlichting formula for turbulent boundary layer on a flat plate), the first cell height (to have $y^+ = 1$) and the cell growth ratio ($= 1.08$). Approximately, the resulting number of elements is around 750,000.

The open-source SU2 flow solver v6.2.0 [7], developed at Stanford University, has been used for RANS analyses. The JST scheme by Jameson, Schmidt and Turkel (2^{nd} order, central flux discretization with addition of artificial dissipation) has been selected to solve the conservative variables, while a 2^{nd} order upwind scheme has been used to solve the Spalart-Allmaras turbulent variable. An Euler implicit time scheme has been used to advance the solution in pseudo-time towards steady-state with an adaptive CFL number ranging from 2 to 50. Convergence has been assumed when either a 6-order residual drop has been reached for all equations or all residuals are lowered below 10^{-8}.

The optimization task has been split into two steps: the first was aimed at quickly exploring the design space with a global algorithm to find a sub-optimal solution, and the second targeted a refinement of the solution. In the initial phase, the Efficient Global Optimization (EGO) algorithm [8, 9] was launched to perform a balanced search of the design space by means of a Kriging surrogate model assisted by the Expected Improvement Maximization criterion. This choice has been driven by the limited dimension of the design space, which makes such an algorithm very effective. The design space was initially sampled with 36 Latin Hypercube Sampling points and then 86 EGO iterations were performed. Starting from the EGO best solution, a Covariance matrix adaptation evolution strategy (CMA-ES) [10, 11] evolutionary search has been launched with a population size of 12 candidates. This phase has required further 268 CFD evaluations of design candidates.

Optimization results are summarized in Table 2 in terms of objective function values and measures of lift/drag curve contribution. For the sake of completeness, even if during the optimization iterations the CFD simulations have been carried out with the Spalart-Allmaras turbulence model, the candidates under analysis (baseline, EGO and CMA-ES optima) have been further analyzed with the $k - \omega$ SST model. Results show that the optimization trend is well captured even by the SST model: both EGO and CMA-ES optima exhibit superior aerodynamic performances with respect to the reference shape. The $k-\omega$ SST turbulence model is in line with the optimization results and is more conservative in predicting the aerodynamic performance of the three-element airfoil in high-lift conditions. The chosen optimization strategy has proven to be successful as the global algorithm recovered the most significant aerodynamic issues of the reference shape while the CMA-ES algorithm worked to push the lift curve towards the "utopia" point while securing the drag levels.

Figure 12 depicts the optimized shapes as compared to the reference one. As a result of the design process, the optimized Krueger elements present a narrower gap and a steeper setting. The bullnose contour is thicker and more rounded, which strongly contributes to increasing the maximum lift and the stall angle. The EGO optimum features the shortest panel length and the steepest setting: this design feature seems to be in partially opposite trend with respect to

ID airfoil	Spalart-Allmaras			$k-\omega$ SST		
	f_{obj}	$\mu(\Omega_L)$	$\mu(\Omega_D)$	f_{obj}	$\mu(\Omega_L)$	$\mu(\Omega_D)$
Baseline	18.893	8.657	1.23	28.016	11.670	1.635
EGO optimum	7.266	4.830	0.244	8.039	5.412	0.263
CMA-ES optimum	6.391	3.993	0.239	7.050	4.283	0.277

Table 2: Summary of CIRA optimization results.

the final solution, i.e. the CMA-ES optimum, and may suggest a multi-modal behavior, which makes the optimal solution not unique.

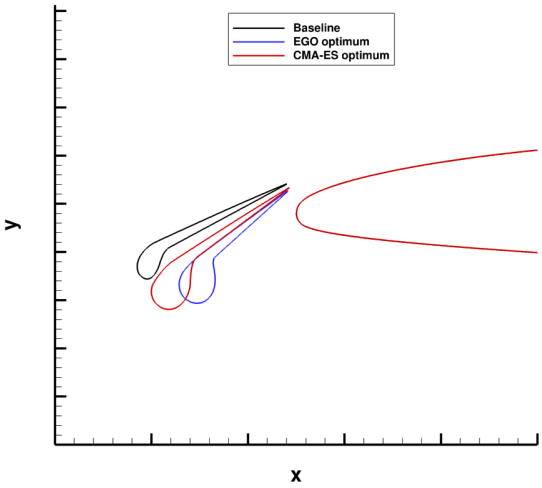

Figure 12: Comparison of reference baseline and optimized shapes.

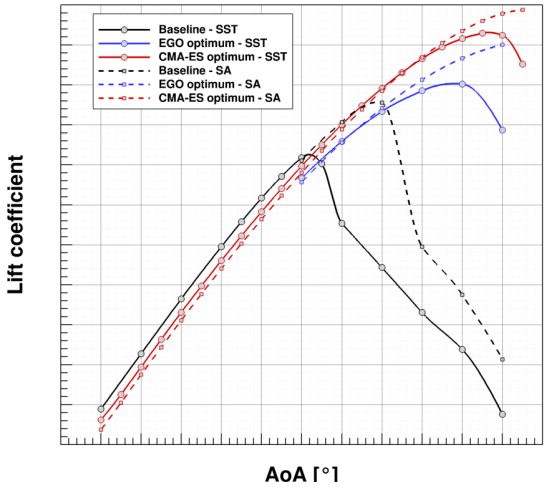

Figure 13: Lift coefficient curve versus angle of attack for baseline and optimized shapes, Spalart-Allmaras (SA) and $k-\omega$ SST (SST) turbulence models.

Figure 13 shows the lift coefficient curve versus the angle of attack for reference and optimized Krueger shapes as computed by using both Spalart-Allmaras and $k-\omega$ SST turbulence models. In order to be consistent with the data shown in the next section about Krueger shape synthesis, the aerodynamic coefficients have been scaled to unit reference length. In the linear range, a slight lift loss is observed, while at higher angles of attack the flow separation on the suction side of the Krueger element is recovered and the lift levels are significantly enhanced. The baseline $c_{L,max}$ is 3.43 at 14° angle of attack ($c_{L,max}$ = 3.71 at 18° angle of attack with the Spalart-Allmaras model). As regards the CMA-ES optimum, the $c_{L,max}$ predicted with the SST model is 4.06 at 23° angle of attack ($c_{L,max}$ = 4.17 at 25° angle of attack with Spalart-Allmaras model).

In Figure 14 the aerodynamic flow field (Mach number contour map) is shown at 18° angle of attack for reference and CMA-ES optimum shapes with both turbulence models employed. This angle of attack has been selected because it illustrates quite well two main outcomes of

the reported task. On one hand, the suppression of the flow separation on the Krueger slat suction side is clearly highlighted as main design feature (e.g., looking at the figure from top to bottom); on the other hand, it shows some discrepancy in the flow prediction when changing the turbulence model (e.g., looking et the figure from left to right), as the SST model predicts a slight early stall.

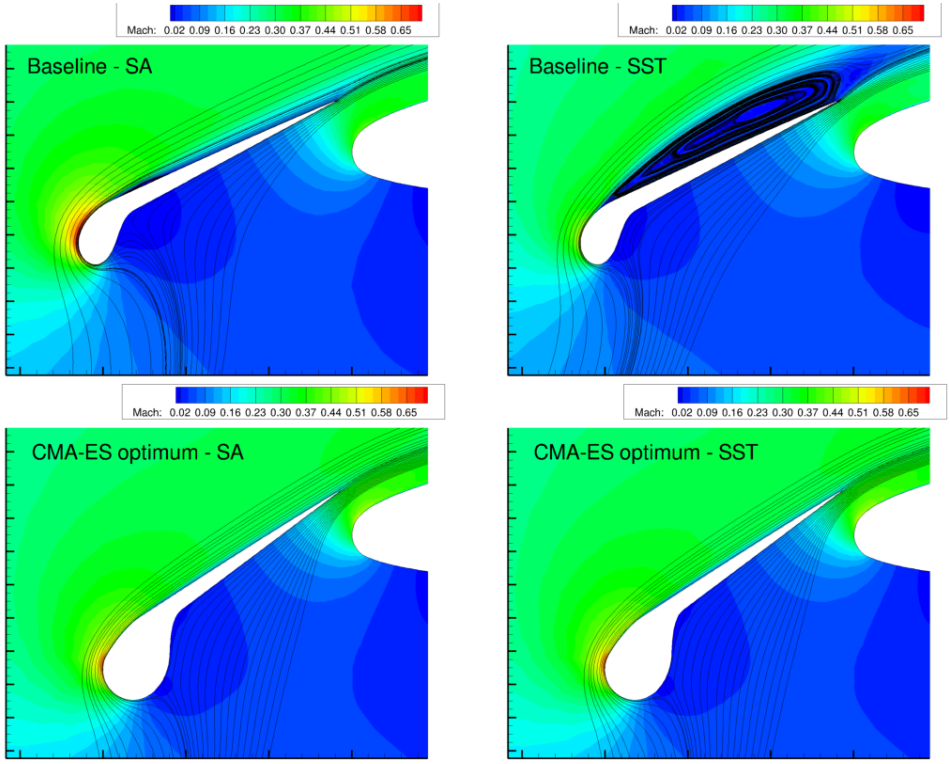

Figure 14: Mach number contour map and flow streamtraces for reference and optimized shape at 18° angle of attack, Spalart-Allamaras (SA) and $k-\omega$ SST turbulence models.

2.5 Comparison of designs

In this section, a cross-check analysis between DLR and CIRA designs is proposed. Before entering into the detailed analysis, a brief synthesis of the main differences between the optimization approaches adopted by the two partners is given here:

CFD method: DLR employed the in-house FLOWer multi-block structured solver, CIRA used the open-source SU2 unstructured solver;

Geometry parameterization: DLR used a CAD-based approach with 12 parameters, CIRA used a CAD-free approach with 5 parameters. In both cases, the panel length and deflection angle are not free parameters and are driven by kinematic feasibility. The main difference is related to the bullnose parameterization: DLR allowed free variation of the design parameters, CIRA explored a more limited set of allowable shapes in order to avoid issues with the Krueger stowage in retracted position. Of course, the attained performance is impacted as

well, as detailed later on;

Geometry detail: DLR optimization took into account the aerodynamic effect of the Krueger open cavity shape, CIRA modeled the main airfoil with closed cavity;

Optimization problem: DLR optimized for a linear combination of maximum lift and climb speed, CIRA defined a maximization problem along the higher branch of the polar curve while also taking into account the drag characteristics;

Optimization algorithm: DLR used the simplex method, CIRA performed a surrogate-based global optimization first, followed by an evolutionary search.

The aim of the crosscheck analysis is to quantify the impact of the CFD code and of the mesh type on the optimal lift curve prediction. Moreover, as DLR performed the design by including the Krueger open cavity shape within the CFD model while CIRA did not consider it, it is deemed interesting to understand if such difference may have an impact on the design. Table 3 provides information about selected crosscheck cases. The following comparative analyses are envisaged:

1. Code to code crosscheck: cases 2, 3, 5 and 6 are compared to investigate the effect of the CFD approach (CFD code and mesh type) on the aerodynamic performance of optimal candidates;

2. Krueger cavity check: cases 1, 2, 4 and 5 are selected to investigate the effect of the Krueger cavity.

Case ID	Geometry	Cavity included (Y/N)	Mesh	Solver
1	CIRA optimum	N	Quad-tri unstruct.	SU2 (SST)
2	CIRA optimum	Y	Quad-tri unstruct.	SU2 (SST)
3	CIRA optimum	Y	Multi-block struct.	FLOWer (SA)
4	DLR optimum	N	Quad-tri unstruct.	SU2 (SST)
5	DLR optimum	Y	Quad-tri unstruct.	SU2 (SST)
6	DLR optimum	Y	Multi-block struct.	FLOWer (SA)

Table 3: Selected cross-check cases.

Figure 15 shows the two comparative analyses. On the left-hand side, the lift curves for cases 2, 3, 5 and 6 are drawn. The general agreement is good both in terms of quantitative comparison and trend capturing. The DLR CFD approach predicts higher lift slopes and slightly higher $C_{l,max}$ with respect to CIRA CFD approach for both DLR and CIRA optima. Likewise, the stall angle of attack for CIRA airfoil is predicted at 22° compared to 23°. At low angles of attack, code-to-code discrepancies seem to be mildly amplified.

On the right-hand side of Figure 15, the lift curves for cases 1, 2, 4 and 5 are reported. The effect of the Krueger cavity on the aerodynamic performance can be considered negligible for both CIRA and DLR shapes. Some additional details are provided in Figure 16 and Figure 17, where the pressure coefficient is compared at low (= 8°) and high (= 24°) angle of attack. DLR optimized Krueger shape is larger than CIRA's; hence the contribution of the Krueger element

to the lift generation is more important. CIRA shape, indeed, partially recovers this feature thanks to higher local curvature and increased loading. Figure 17 confirms that the aerodynamic disturbance related to the open cavity is purely local and therefore negligible at both low and high angle of attacks.

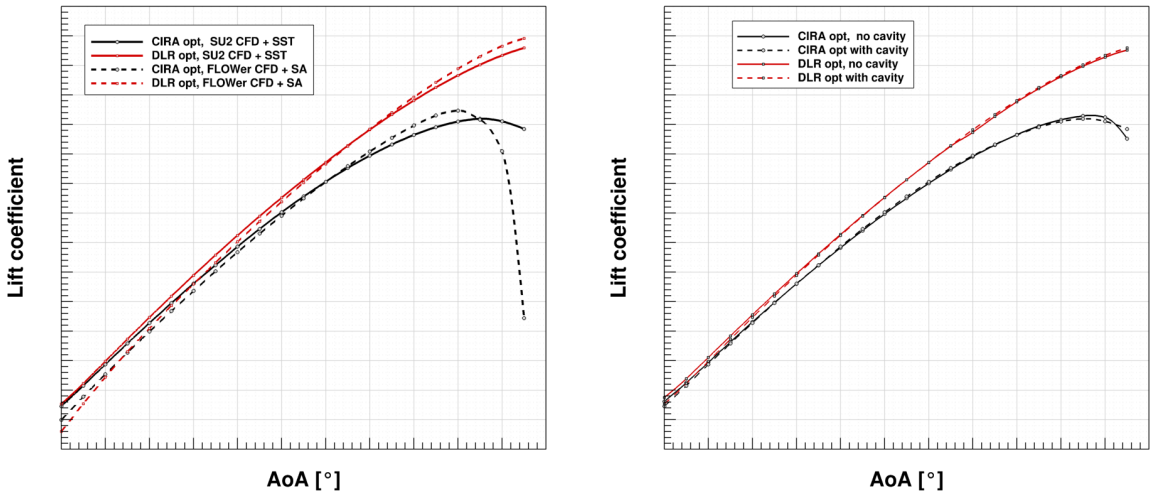

Figure 15: Lift coefficient vs angle of attack for CIRA and DLR optima, impact of CFD approach (left) and Krueger cavity (right).

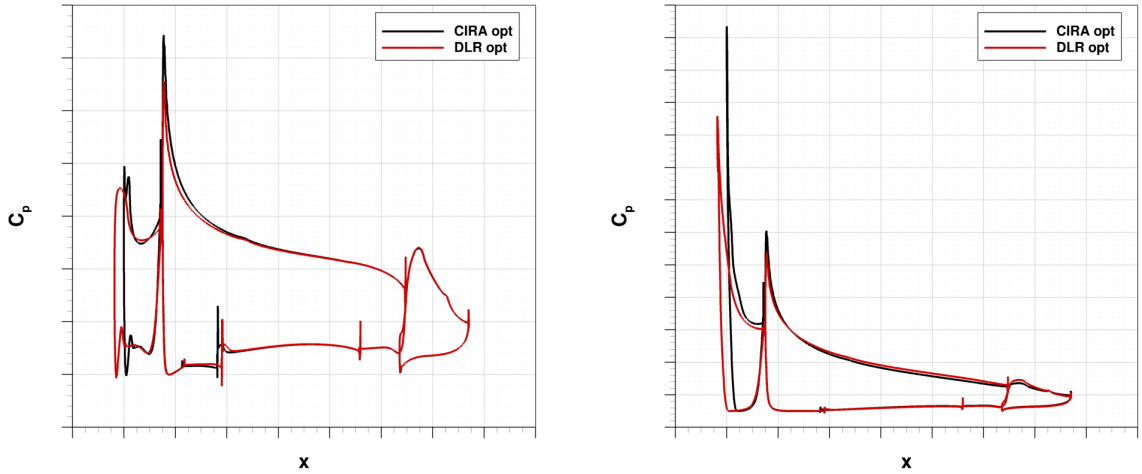

Figure 16: Pressure coefficient comparison between CIRA and DLR optima, AoA= 8° (left) and 24° (right).

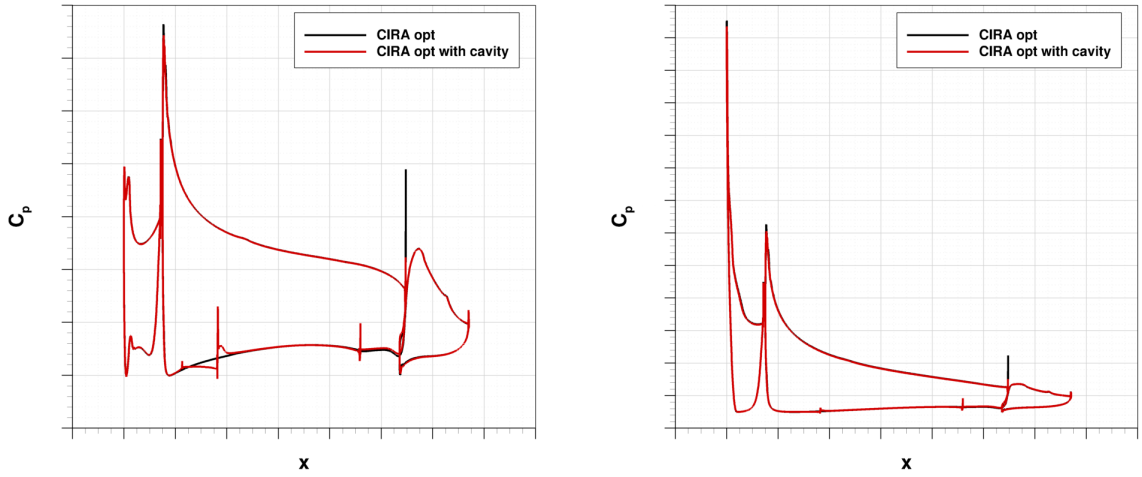

Figure 17: Pressure coefficient comparison with and without cavity, AoA= 8° (left) and 24° (right).

3 KRUGER DEVICE SHAPE SYNTHESIS

After the initial concurrent design phase, both obtained optimum solutions have been compared in detail. In the analysis, the following aspects were identified

- The Krueger panel of the DLR design is too long as it violates the front spar clearance constraint and even penetrates the front spar itself. This glitch has been introduced already in the initial configuration while porting the AFLoNext design to the DLR-F15-LLE shape. The AFLoNext configuration had a front spar located more downstream and in the setup of the DLR-F15 this has not been corrected to the corresponding front spar location
- DLR used the older and stronger impact shielding requirement of 7° impact at a geometric 6° angle of attack. CIRA implied in their design the relaxed 9° impact angle. Further on, CIRA respected that the geometric angle of attack for a wing section of a swept wing is increased by $\tan \alpha_{2D} = \tan \alpha_{3D} / \cos \theta$. For an assumed wing sweep of $\theta = 30°$ the reference angle of attack is for the 2D airfoil section $\alpha_{2D} = 6.92°$. The relaxed shielding requirement allows for a lower position and a steeper deflection closer to 140°, which is assumed to be beneficial.
- The CIRA design exhibits an unintended waviness on the upper side of the Krueger bull nose, which is generated by the use of Hicks-Henne functions and their connection to the rigid Panel shape on the upper side.

In a first synthesis, it was therefore decided to orient at the CIRA design but to reshape the bull nose to a smoother shape. To achieve this, The CIRA design was reparametrized using DLR's design parameters. Figure 18 shows a comparison of the original design shapes and the synthesized design, with a close-up to the bull nose shape. It is seen that the DLR parameterization nicely rebuilds the CIRA design with a smooth bull nose shape.

Figure 19 shows a comparison of the lift coefficient of these designed configurations. The lower performance of the CIRA design can be mainly attributed to the shorter panel and the resulting

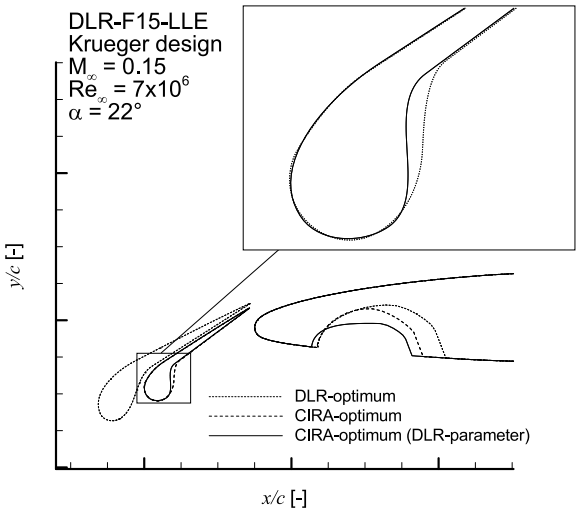

Figure 18: comparison of the Krueger flap shapes obtained by DLR and CIRA design optimization together with the reconstructed CIRA design using DLR's parameterization approach.

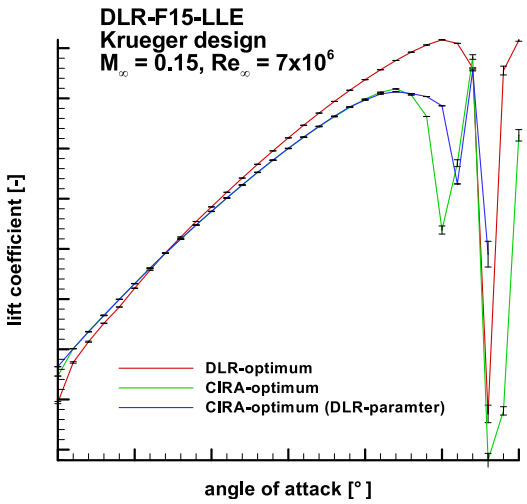

Figure 19: comparison of the lift coefficient versus angle of attack for DLR and CIRA designs and the reconstructed CIRA design using DLR's parameterization approach.

smaller increase in effective airfoil chord with deflected Krueger. The smoother bull nose shape obtained by the re-parameterization is seen in the smoother stall behaviour at a similar maximum section lift coefficient. The rebuilt shape therefore retains the positive performance established by the original CIRA design. The shortfall in maximum section lift coefficient compared to the original DLR design is acceptable. On the one hand, the DLR designed Krueger is far too large and penetrates the front spar. On the other hand, it is not the purpose of this work to design the ultimate Kreuger design but to provide a reasonable Krueger device with a high performance. A maximum section lift coefficient of above 4 is still a high-performing high-lift airfoil design.

Figure 20 shows a comparison of the pressure distributions for all three designs at an angle of attack close to stall of the CIRA design. Again, the reproduction of the CIRA design by the DLR parameters is good in general. At the Krueger a slightly lower suction peak is visible showing the effect of the smoother bull nose shape.

4 KRUGER DEVICE SHAPE ALIGNMENT TO KINEMATICS REQUIREMENTS

The initial Krueger device and the synthesized design have been analysed in UHURA by ASCO regarding the feasibility of the corresponding kinematics [12]. While all the initial requirements have been met by the synthesized design, two new issues showed up, which would not prevent integration but a slight change would provide high benefits for the integration. At first, a longer Kruger panel in terms of the downstream edge would avoid an otherwise necessary cut-out in the lower skin allowing passage of the drive lever arm. At second, a cut-off of the rear bull-nose shape would allow for a higher retraction angle of the bull nose, which in turn would reduce the space allocation and provide a strengthening of leading edge ribs to support the aerodynamic loads on the leading edge. The design was changed accordingly by reducing the

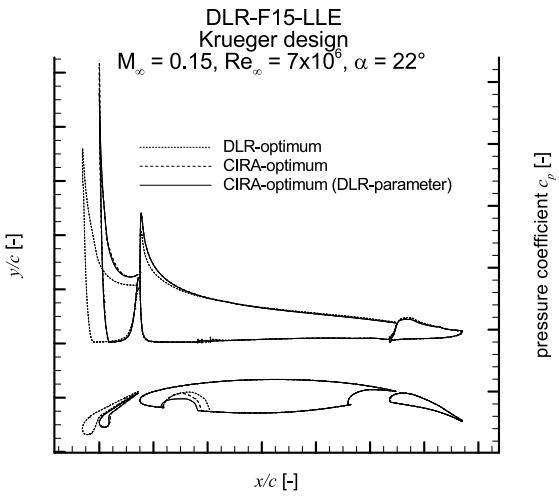

Figure 20: comparison of the pressure distributions for DLR and CIRA designs and the reconstructed CIRA design using DLR's parameterization approach.

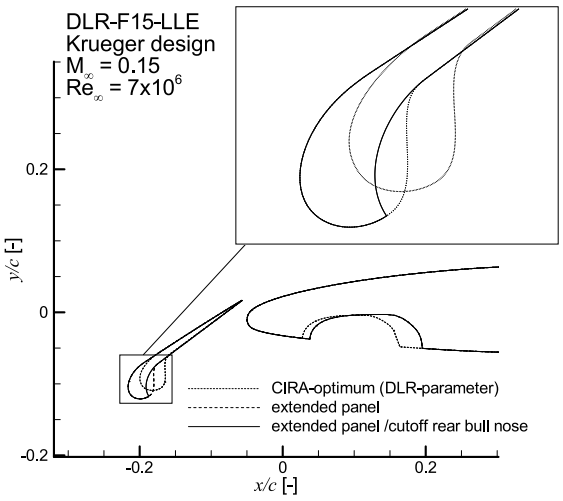

Figure 21: final changes at Krueger design to incorporate refined requirements from kinematics integration.

offset to the downstream Krueger edge to the front spar to a minimum of 0.5%c. The rear shape of the bullnose was changed. The GC2-continuous spline was replaced by a sharped edge connection. Figure 21 shows the adopted geometry with a close up to the changes Krueger leading edge. Within this iteration, the hinge point has additionally been refined to even more closely correspond to the CIRA-design based position of the Krueger device in deflected position.

The change in aerodynamics is shown in Figure 22. In general, the extension of the Krueger panel leads to a sharper wing stall at a slightly increased maximum lift coefficient, which probably may be prevented by a less swallow deflection. The cut-off of the rear bull nose reduces stall incidence by 1 degree with a slight reduction of maximum lift coefficient. The maximum lift coefficient of the final design is similar to the optimal CIRA design value.

Figure 23 compares the pressure distributions at a high angle of attack close to the maximum lift coefficient. The extension of the panel is accompanied by a slight reduction of the suction peak but at a similar pressure gradient. At the main wing the pressure rise past the suction peak is visibly steeper while the suction peak level is unchanged. The cut-off of the rear bull-nose has no significant effect on the pressure distribution.

As the aim of the task was to provide a reasonable Krueger device at a high aerodynamic performance, it is judged by all partners that the obtained result is sufficient for the aim of the project. The Krueger device shows a high maximum lift coefficient at a high corresponding stall angle. Compared to the initial configuration, a premature stall is prevented. Nevertheless, some potential for a smoother stall onset still exists.

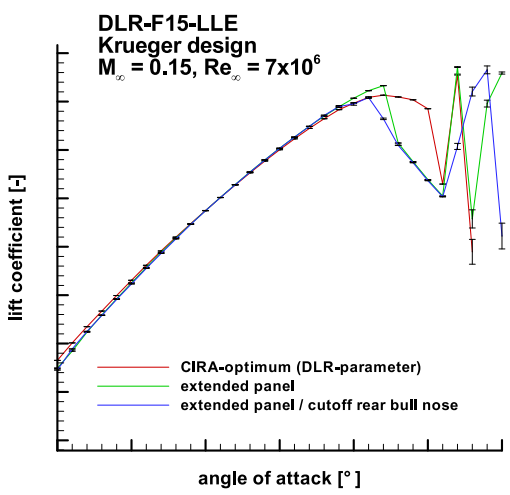

Figure 22: lift vs. angle of attack for the finally refined Krueger device with respect to kinematics requirements.

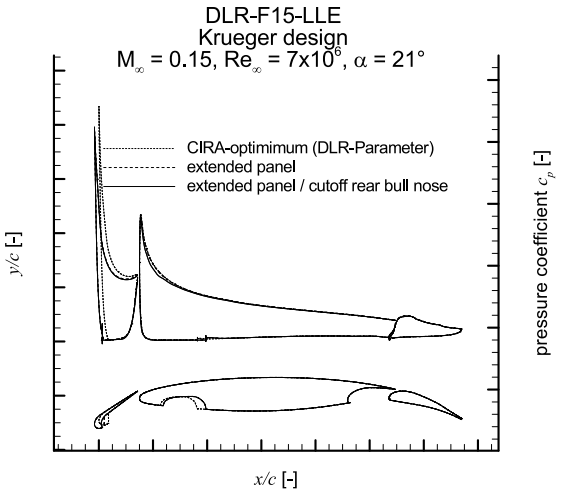

Figure 23: comparison of pressure distributions the finally refined Krueger device with respect to kinematics requirements.

5 CONCLUSIONS

The design optimization work described here can be considered a success both from a methodological point of view and from the results obtained. From the point of view of the optimization method, we opted for a hybrid competitive-cooperative approach in which two UHURA partners, namely DLR and CIRA, first proceeded to an optimization phase in which, independently of each other and interpreting the requirements and constraints of the problem in a slightly different way, they produced two improved solutions compared to the baseline. In the second phase, instead of choosing and judging which of the two solutions was better, they decided to propose a third one that combined the favorable characteristics of both. The advantage of this approach is evident when more complex and computationally demanding problems are to be solved. In these cases, the initial design choices can profoundly influence the final result. The hybridization of two solutions obtained following non-overlapping approaches can improve the design process performance and efficiency. Finally, from the point of view of the results obtained, the design of the Krueger flap has proved to satisfy all the design requirements very well and, as evidenced by the volume of numerical and experimental works produced within UHURA, has allowed a considerable advancement of the technical knowledge on aerodynamic and structural problems inherent in the deployment of high-lift devices.

ACKNOWLEDGEMENTS

The project leading to this presentation has received funding from the European Union's Horizon 2020 Research and Innovation Framework Programme under the research and innovation programme under grant agreement No 769088.

REFERENCES

[1] "UHURA project." `https://uhura-project.eu/`.

[2] H. Strüber and J. Wild, "Aerodynamic design of a high-lift system compatible with a natural laminar flow wing within the DeSiReH project," in *29th Congress of the International Council of the Aeronautical Sciences*, (St. Petersburg, Russia), ICAS, Sept. 2014. ISBN 3-932182-80-4.

[3] D. M. Franke and J. Wild, "Aerodynamic design of a folded krüger device for a HLFC wing," in *19. DGLR-Fachsymposium der STAB*, vol. 2014 of *Mitteilung zum STAB Jahresbericht*, pp. 28–29, November 2014.

[4] J. Wild, "Initial geometry of DLR-F15-LLE with Krueger flap for WP 2," techreport UHURA Coordination Memorandum UH-11-CM03-DLR, DLR, 2018.

[5] J. Wild, "Validation of numerical optimization of high-lift multi-element airfoils based on navier-stokes-equations," in *20th AIAA Applied Aerodynamics Conference*, 2002.

[6] C. Geuzaine and J.-F. Remacle, "Gmsh: A 3-D finite element mesh generator with built-in pre- and post-processing facilities," *International Journal for Numerical Methods in Engineering*, vol. 79, no. 11, pp. 1309–1331, 2009.

[7] T. D. Economon, F. Palacios, S. R. Copeland, T. W. Lukaczyk, and J. J. Alonso, "SU2: An open-source suite for multiphysics simulation and design," *AIAA Journal*, vol. 54, no. 3, pp. 828–846, 2016.

[8] D. R. Jones, M. Schonlau, and W. J. Welch, "Efficient global optimization of expensive black-box functions," *Journal of Global Optimization*, vol. 13, pp. 455–492, 1998.

[9] B. M. Adams, W. J. Bohnhoff, K. R. Dalbey, M. S. Ebeida, J. P. Eddy, M. S. Eldred, R. W. Hooper, P. D. Hough, K. T. Hu, J. D. Jakeman, M. Khalil, K. A. Maupin, J. A. Monschke, E. M. Ridgway, A. A. Rushdi, D. T. Seidl, J. A. Stephens, L. P. Swiler, and J. G. Winokur, *Dakota, A Multilevel Parallel Object-Oriented Framework for Design Optimization, Parameter Estimation, Uncertainty Quantification, and Sensitivity Analysis: Version 6.15 User's Manual*, Nov. 2021. Sandia Technical Report SAND2020-12495.

[10] N. Hansen, "The CMA Evolution Strategy: A comparing review," in *Towards a New Evolutionary Computation: Advances in the Estimation of Distribution Algorithms* (J. A. Lozano, P. Larrañaga, I. Inza, and E. Bengoetxea, eds.), pp. 75–102, Berlin, Heidelberg: Springer Berlin Heidelberg, 2006.

[11] N. Hansen and A. Ostermeier, "Completely derandomized self-adaptation in evolution strategies," *Evolutionary computation*, vol. 9, no. 2, pp. 159–195, 2001.

[12] A. Vervliet, "Kinematic constraints linked to Krueger panel, actuation and deployment mechanisms," Tech. Rep. UHURA Deliverable D12-1, ASCO, 2019.

[13] J. Wild, "Loads on the initial DLR-F15-LLE Krueger flap," techreport UHURA Coordination Memorandum UH-11-CM05-DLR, DLR, 2018.

[14] V. Ciobaca and J. Dandois, "High reynolds number high-lift airfoil testing with flow control," in *35th AIAA Applied Aerodynamics Conference*, 2017.

[15] J. Wild, *High-Lift Aerodynamics*. CRC Press, 1st ed., Feb. 2022.